3D Digital Modeling and Identification of Pavement Typical Internal Defects Based on GPR Measured Data

Abstract: A three-dimensional array ground-penetrating radar (GPR) technology can non-destructively obtain internal pavement distress characteristics. However, interpreting radar images and data analysis is challenging. To improve the accuracy of distress identification, a three-dimensional digital model of internal pavement distress was established. Firstly, the collected electromagnetic signal raw data were pre-processed to effectively eliminate spurious signals and enhance distress characteristic signals. The distress was located, and the radar GPR images of typical distress were extracted and summarised. Next, the 3D dataset was constructed based on the pre-processed electromagnetic echo signals. A 3D digital model of internal pavement distress was generated using the inverse distance weight method and ray-casting method with trilinear interpolation. Finally, relying on the physical project, cores were extracted to validate the distress model. Research results show that the method effectively reflects the internal pavement distress characteristics, and the constructed model can realize the interactive images between the pavement entity and the digital model, which can essentially contribute to the digital twin of pavement systems.

Keywords: Road engineering; Pavement detection; Digital twin; Pavement internal defects; 3-D array ground penetrating radar

1. Introduction

At present, the total mileage of highways in China exceeds 5.2 million kilometres, and with the total mileage and density of highways increasing yearly(Guo et al., 2022), highway maintenance gradually becomes the focus of work to ensure the normal operation of traffic(Li et al., 2022). Rapid detection and evaluation of pavement health status is an important prerequisite for carrying out maintenance work(Hou et al., 2021). With the rise of computer technology in the early 21st century, automatic detection technology based on image recognition processing has flourished(Liu et al., 2022), as attested by the fact that infrared cameras(Saponaro et al., 2014), photometric stereoscopic techniques, and thermal infrared imaging can visually obtain pavement performance traits. However, these technologies are limited as they do not reflect the internal pavement distresses and can only be applied when internal distresses have developed to the road surface(Tello-Cifuentes et al., 2023). Ground penetrating radar (GPR) technology is promising in detecting sub-surface conditions. The principle of the GPR technology is based on sending electromagnetic waves toward the target and receive reflections from the mismatch of electrical properties between sub-surface materials. The reflection amplitudes and two-way travel time of the received EM waves are used to analyze the geometrical and electrical properties of the sub-surface materials. The current stage of engineering practice shows that GPR has become an important method on road inspection to obtain accurate information of the pavement internal structure condition partly because of its easy operation and fast detection process(Walubita et al., 2009). Radar inspection data provide important supports for evaluating the service condition of pavement and analyzing the causes of distress, and also provide the possibility of constructing a digital twin system for internal pavement distress (Breysse, 2012).

Kassem et al.（2008) has demonstrated that GPR can be used to detect road compaction using X-ray CT. Ameri has confirmed the GPR measures density more accurately than the PQI(Ameri et al., 2014). Sivagnanasuntharam et al., (2023) reviewed the principle and current status of ground penetrating radar used in road density and asphalt compaction detection. The effectiveness of ground penetrating radar in this aspect is demonstrated. With the deepening of the understanding of electromagnetic technology, experts began to explore other uses of ground-penetrating radar in the field of pavement. By analysing radar signals, combined with coring and laboratory measurements, Li et al., (2015) demonstrated that GPR can accurately assess compaction uniformity, and identify localized voided areas and debonding problems. It shows that ground-penetrating radar can be used as an effective non-destructive assessment equipment in the field of pavement detection. At present, ground-penetrating radar is mainly used in road engineering to detect thickness density(Dong et al., 2019) and internal pavement distress (Wang & Al-Qadi, 2022).

For the detection and identification of internal pavement distresses, there are three main types of methods: expert interpretation of profile, signal analysis, and image processing with artificial intelligence classification and identification (Wang et al., 2021). Meanwhile, with the development of 3D array radar technology, the multi-profile integrated interpretation and 3D imaging help to improve the accuracy of distress identification. Guo et al., (2019) proposed a multi-profile integrated interpretation method to compare the differences and correlations between ground-

69 penetrating radar profiles of adjacent lanes. Eliminating interference quickly and
70 reducing the multiple interpretations, the method effectively improves the accuracy of
71 road subsurface distress interpretation. However, the use of empirical identification
72 method of profiles often leads to the problems of unclear radar images, difficult data
73 interpretation, and subjective dependence (J. Zhu et al., 2023).

74 At present, there are lots of theories and technologies regarding 3D array
75 ground-penetrating radar, and radar images feature analysis and core verification of
76 internal pavement distress have been carried out (Soldovieri et al., 2007). To present
77 the internal condition of the measured object more intuitively, domestic and foreign
78 scholars also try to visualize the radar underlying data Soldovieri et al., (2007) uses a
79 microwave-tomography-based solution algorithm tailored to process radar signals to
80 solve the problem of inverse scattering of electromagnetic signals. The effectiveness
81 of this method for 2D radar images reconstruction is demonstrated. In order to give
82 full play to the advantages of 3D GPR data, many scholars directly use 3D data for
83 interpolation modelling from the perspective of visualization. Yan (2023) used
84 ordinary kliking and cubic spline interpolation methods to carry out in-channel
85 interpolation, establish three-dimensional highway geological bodies, and realize
86 three-dimensional reconstruction of GPR data. For the optimization of digital model
87 rendering after interpolation, the method in the form of isosurface is widely used.
88 Forte et al., (2021) interpolated between adjacent slices with Matlab, extracted
89 isosurface semi-automatically, and defined the plane position and volume of the target
90 at the same time, and established the corresponding relationship between signal

features such as amplitude and phase and isosurface threshold. Theoretically, the influence of the surrounding environment of the underground object on the detection result is over come. Lee et al., (2022) scanned the underground cavities beneath the pavement layer, and the 3D digital model of underground cavities was constructed by a digital cavity imaging system. Pereira et al., (2020) first combined the Hessian-based enhancement filter with the time-domain back-projection algorithm (BPA) for processing air-coupled radar data, which reduced the background noise and highlighted the 3D images of the pipes. It was successfully applied to three laboratory experimental scenarios of buried plastic pipes with different sizes and shapes. However, the actual scenario of radar scanning is that the pipes are embedded in concrete, rocks, etc., presenting an important challenge in processing the reflected signals from the surrounding media. Despite this, there is still little relevant research on the three-dimensional modelling and display of pavement internal distress.

In the field of road engineering, to improve the detection accuracy, it is often necessary to extract cores several times to verify the detection result and accumulate rich practical experience (Rasol et al., 2022). However, due to the complex diversity of internal pavement distress, the core samples taken can hardly fully characterize all types of working conditions.(Hugenschmidt & Herlyn, 2014). In contrast, based on the underlying radar signal data, analysing the characteristics of radar signal data directly and establishing 3D digital models of pavement internal distress will be more helpful to grasp the characteristics of pavement internal distress.

Digital twin technology can establish the data connection between the real and digital worlds through the interactive images of the real world and the digital world(Thelen et al., 2022), data fusion and analysis, and iterative optimization of decision making. Based on multi-dimensional data analysis, digital twin feature models are built by using this technology to achieve performance prediction, risk assessment, and conservation decisions in specific scenarios(Holopainen et al., 2022). Digital twins have started to be applied in industry, construction, and transportation(Menon et al., 2023), but the application in road inspection is comparatively sparse(Cruz et al., 2022).Ground-penetrating radar-based detection identification and display technology provide a good foundation for building a digital twin model of pavement internal distress(Morsy & Shaker, 2022), but little research has been carried out on it.

Therefore, in order to improve the readability of the radar images, get rid of the dependence on expert experience interpretation, and improve the work efficiency of using GPR to detect the internal distresses of pavement, this paper presents the internal distresses of pavement with three-dimensional digital models, and relying on physical engineering, research on the refinement of pavement internal distresses identification based on 3D digital modelling was carried out. The characteristics of distress images was analysed, the underlying radar signal data behind the images was extracted, and a typical 3D digital model of the distress was established. Combined with the results of coring at corresponding locations, the constructed 3D digital models of pavement internal distress can visualize the internal structure of pavement and distress characteristics in three dimensions. The interactive images between pavement entities and the digital world were realized, thus accurately identifying multiple distress types and their ranges. The research results can also lay the foundation for accurately images the dynamic development pattern of road distress and for the road's whole life cycle maintenance decisions.

2. 3D Array Ground Penetrating Radar System

To **achieve a breakthrough**, including the low efficiency of traditional ground-penetrating radar single-channel **testing** and the great difficulty in feature identification of two-dimensional radar images, three-dimensional array ground-penetrating radar products have increasingly become the mainstream form of ground-penetrating radar non-destructive testing. With multiple-input and multiple-output (MIMO) antenna architecture, the array radar achieve multiple test channels of electromagnetic wave transmission/reception within the physical dimensional coverage width of the radar(Syeda et al., 2021), and the radar data from all test channels are subjected to array radar signal processing, thereby generating 3D detection data.

This paper adopts the domestic independent intellectual property rights GER-A900A14RS three-dimensional ground-penetrating radar system as shown in Figure 1. With the GPS system, the radar slice images are tiled onto the images according to the detection track, thus achieving full coverage detection of pavement and accurate location of internal pavement distresses, as shown in Figure 2. Measured data were collected from a highway in Jiangsu Province with the antenna center frequency 1200MHz. Vertical feature recognition accuracy is higher than 3.2mm whilst the and horizontal feature recognition accuracy allows for detecting the width of a gap greater than 4mm, less affected by the road material dielectric constant. There are 7 transmitting antennas (7T), each corresponding to 2 receiving array elements (14R), in other words, there are 14 test channels of echo data in total, as shown in Figure 3. The equipment relies on a number of expressways in Jiangsu, Shandong, Jiangxi and other provinces to carry out a total of more than 1000km of measured data acquisition and coring verification work. Taking the test results of Rylan Highway in Shandong Province as an example. We calculated the proportion of each distress separately as shown in Figure 4. it can be fully demonstrated that the equipment can be effectively used in the detection of pavement internal distress.

Figure 1. GER-A900A14RS 3D Ground Penetrating Radar Equipment

Figure 2. Section Fusion Diagram of Road Line Measurement and Track Detection

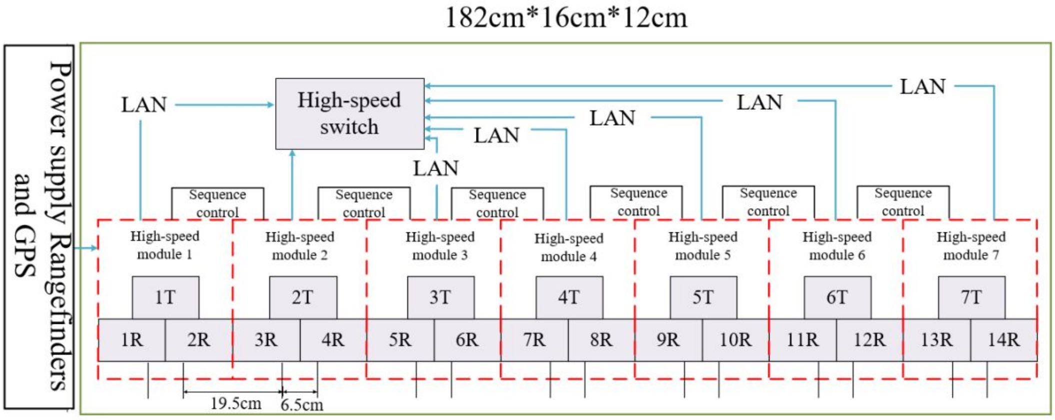

Figure 3. Layout of Array Radar Antennas

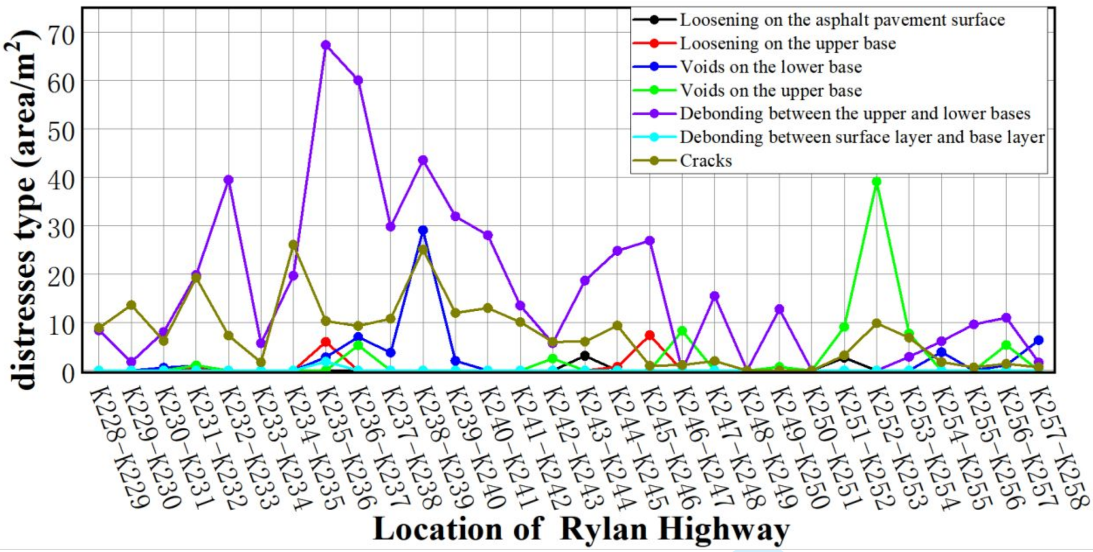

Figure 4. Results of Distresses Detection of Rylan Highway

3.Radar detection data processing method

The radar images directly obtained by field detection basically does not contain any effective information, and useful signals are covered by interference signals in the detection process. Therefore, we need to go through a series of radar signal preprocessing processes to make the radar images clear and highlight the distress characteristics in the images. In this section, the radar images characteristics of various distresses are also summarized, which will be helpful to distinguish the internal diseases of different pavement according to the images.

3.1 Pre-processing of signal data

When radar detects the target, the useful signals are disturbed by clutter and noise(Breysse, 2012). In this paper, the array radar data is pre-processed as follows to suppress the noise and improve the signal to noise ratio.

(1) Zero-bias treatment

Because the array radar hardware circuit sometimes has an unbalanced voltage, the echo signal has a DC offset, resulting in the echo deviation from the zero-reference line, that is, the asymmetry of positive half cycle and negative half cycle will appear in the profile of the single-channel waveform A-scan. The DC components should be eliminated or suppressed before other processing of the data. Usually, the single channel waveform data is summed and then divided by the number of sampling points to obtain the average values. Using the channel waveform data to subtract the above mean value can obtain the zero-deviation result, which is expressed by the formula:

$$A'(n) = A(n) - \frac{1}{n}\sum_{i=0}^{N-1} A(i) \tag{1}$$

where *A (n)* is the original single-channel waveform A-scan echo data without processing; *A'(n)* represents the A-scan echo data after zero bias processing; *N* is the number of sampling points of single-channel waveform A-scan, 256 in this paper; *n* is the n^{th} sample in each A-scan.

(2) Zero-point adjustment

Given the integrity of the original data, the transmitting antenna usually has a certain distance from the ground, indicating that the zero position of timing is not set to the ground. In order to obtain accurate distress depth information, it is necessary to adjust the zero point according to the changing time of the relative dielectric constant, in other words, to set the ground position to the zero-timing position.

(3) Gain adjustment

When electromagnetic waves are transmitted downward, the amplitude of the reflected waves decrease with time, due to the absorption of the medium and the energy loss during the electromagnetic propagation and diffusion, so it is difficult to identify the signal of distress in depth directly. Gain regulation of the deep signal of the original signal can improve the images quality and enhance the characteristics of deep distress waveform.

(4) Data filtering

Pulsed ground exploration radar inevitably introduces the electromagnetic component outside the working band, so filtering processing is required to reduce the noise interference outside the working band. Data filter mainly consists of a finite pulse response FIR filter with a linear phase and an infinite pulse response IIR filter with a nonlinear phase. Array radar is dominated by ultra-wideband radar, and the corresponding parameters of the filter should be set according to the working frequency band range. The low and high frequencies selected in this paper are 450MHZ and 1350MHZ, respectively.

(5) Background elimination

After the gain adjustment of the radar data, the reflected wave amplitude increases. Consequently, the uniform and continuous horizontal stationary wave signal increase synchronously, which is not conducive to identification of the target radar signal. Through the background elimination, the influence of horizontal stationary wave can be effectively removed. The processing is to average the specified total echo channel signal, and then each channel data minus the mean of single-channel waveform. The influence of the horizontal fixed wave can be weakened or eliminated, thus highlighting the irregular target signal. The algorithm for noise selection is as follows:

$$\mathrm{x}(\mathrm{t})' = \frac{1}{N_2 - N_1 + 1} \sum_{\mathrm{i}=N_1}^{N_2} \mathrm{x}_{\mathrm{i}}(t) \qquad (2)$$

where N_1、N_2 are the start and end channels of background noise in the selected interval of distress position; *x (t)'* represents the average single-channel waveform within the selected interval; and *x (t)* is the amplitude of the original channel reflected echo signal.

Background elimination is as follows:

$$y(t) = x(t) - x(t)' \qquad (3)$$

where *y (t)* is a single sub-waveform after each process.

(6) Migration processing

The electromagnetic wave emitted from ground-penetrating radar will cover a certain space angle, so the reflection characteristics of the target can be detected both near and away from the distress feature. Meanwhile, the original information of the distress characteristics can be recovered by the migration processing of GPR, the algorithm is mainly divided into two types: diffraction migration based on ray theory and migration based on wavefield extrapolation. Among them, the migration method based on ray theory lacks amplitude and dynamic information, and produces poor return effect of reflector under complex geological conditions. Based on the wave field extrapolation, methods includes finite difference, frequency-wavenumber domain migration, and Kirchhoff integral, which are based on the wave equation, maintain the characteristics of the reflection wave during the migration process, resulting in high imaging accuracy(W. Zhu et al., 2020). Currently, the most mature method is Kirchhoff integral migration, which can adapt to irregular observation systems and reflect interfaces at any inclination angle. It has flexible requirements for profile grids, high computational efficiency, fast data processing speed, and is suitable for road structures with relatively uniform media. However, this process is only suitable for the distresses with small lateral velocity changes in the signal. It is not suitable for loose, empty, and poor interlayer bonding distress with large distress ranges and intuitive spectrum representations in practice. Therefore, this process is only applied to the processing of signal of small-sized crack distress. Using the Kirchhoff diffraction integral formula (Formula 4), the energy from each channel coming from the same diffraction point is backscattered and placed on the corresponding physical diffraction point underground.

$$u\left(x,y,z,t\right)=-\frac{1}{4\pi}\oint_{Q}\left\{[u]\frac{\partial}{\partial n}\left(\frac{1}{r}\right)-\frac{1}{r}\left[\frac{\partial u}{\partial n}\right]-\frac{1}{Vr}\frac{\partial r}{\partial n}\left[\frac{\partial u}{\partial t}\right]\right\}d_{Q} \quad (4)$$

where Q is the closed curve of the surrounding point (x, y, z); n is the external normal of Q; r is the distance from (x, y, z) points to Q; [] represents the delay bit; $[u]=u\left(t-\frac{r}{V}\right)$; $u(x,y,z,t)$ is the true profile of the tested area.

The migration is treated as an inverse problem, so the time is "backward" to the time t=0, converting the delay bit to the lead bit, thus determining the cross section. The spatial depth z is converted to the temporal depth t0. The Kirchhoff migration formula is obtained as follows:

$$u\left(x,t_0,t=0\right)=\frac{1}{2\pi}\oint_{x}\left\{[u]\frac{\partial}{\partial z}\left(\frac{1}{r}\right)-\frac{1}{V_r}\frac{\partial r}{\partial z}\frac{\partial}{\partial r}\right\}u_{(x_1,0,\tau)}d_{x} \quad (5)$$

where $t_0=2z/v$; $\tau=\left[t_0^2+\frac{4(x-x_l)}{v^2}\right]^{1/2}$; xi is the ground record track abscissa; the post-migration section track abscissa is represented by x; $r=\left[z^2+(x-x_l)^2\right]^{1/2}$.

The radar images of four typical distresses were established after data processing, as shown in Table 1 below:

Table 1. Comparison data processing

Types of distress	Radar images before data processing	Radar images after data processing
Cracks		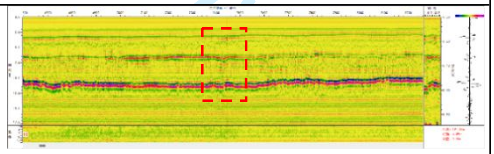
Voids	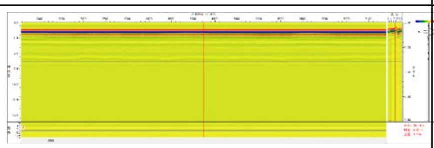	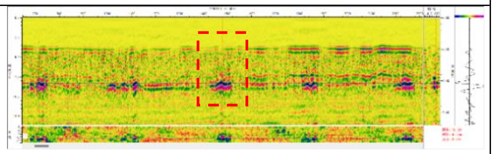
Loosening	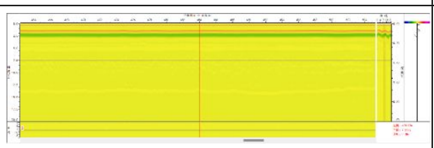	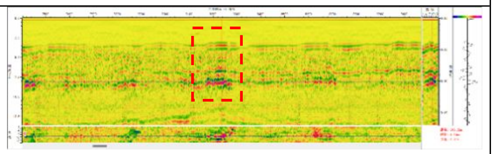

Debonding	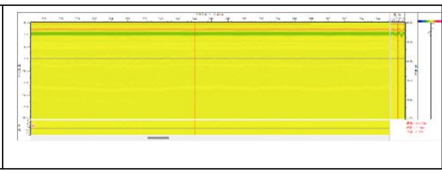	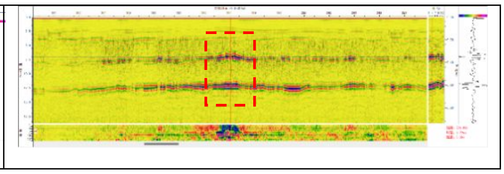

3.2 Typical distress images characteristics

Through the above data processing, the clutter was effectively removed, highlighting the images characteristics of each distress. Analysis of the radar images of typical distresses is helpful to locate the abnormal position of the road internal structure quickly and accurately to then determine the distresses type preliminarily. Due to the dielectric differences among the paving materials used at the surface layer, the upper base, and lower base, reflected waveforms are obvious at the interfaces of different structures. The road structure with defects usually has water, air and other media inside, and its electromagnetic reflection will show different waveform characteristics. This paper conducted ground-penetrating radar detection based on a highway in Jiangsu, Jiangxi, and Shandong Provinces, with the detection mileage of 1000 kilometers. Cores were extracted at 60 positions where the waveforms were abnormal, the distress types were scaled, and radar images characteristics of four typical distress were elaborated in Table 2.

Table 2. Radar Images Characteristics of Typical Distress

Typical distress	Radar images features
Loosening	The phase axis is in chaos; the reflection waves, in serious condition, will miss or be interrupted.
Debonding between layers	The phase axis is continuous, horizontally; the amplitude of the interlayer connection increases.
Voids	The phase axis is dislocated; the reflection waves are regular strong reflection and the vertical range influence is large.
Cracks	The phase axis is discontinuous; the crack position waveform is convex; the reflection area is hyperbolic.

(1) Loosening

Loosening distress takes the form of honeycomb with pores full of air and water. The large medium difference leads to the disorder of reflected radar echoes and phase axis with irregular clutter interference, wavelength enlargement, and obvious difference in wave group characteristics. The disorder is further aggravated with an increase of the loosening degree, that results resulting in the local loss, dislocation, and interruption of reflected waves.

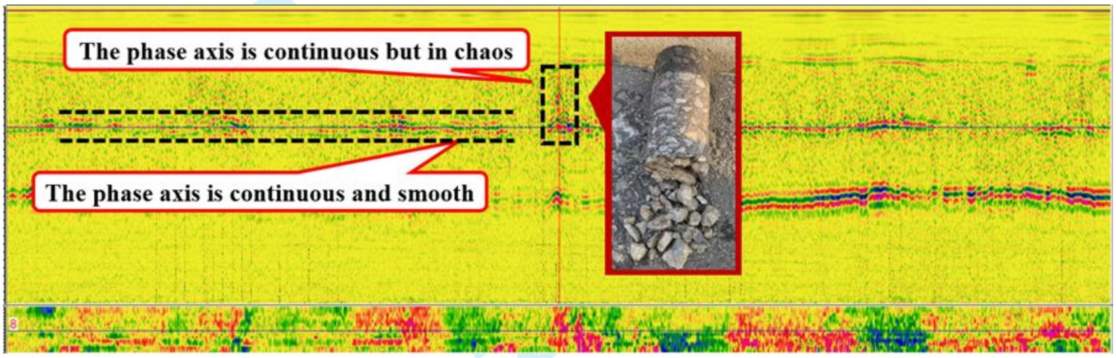

Figure 5. Radar Images Characteristics of Loosing and Corresponding Core

(2) Debonding between layers

Debonding usually occurs between the surface layer and the base layer, and the upper layer and lower base layer (Wang et al., 2022). That is, the two layers of road media are filled with a very thin layer of air or water. In the radar spectrum, the debonding is obviously represented as a strong reflected zone with only a small wavelength change. Its vertical range is small, the phase axis is continuous, and the reflection strength is greater than the position with better bonding.

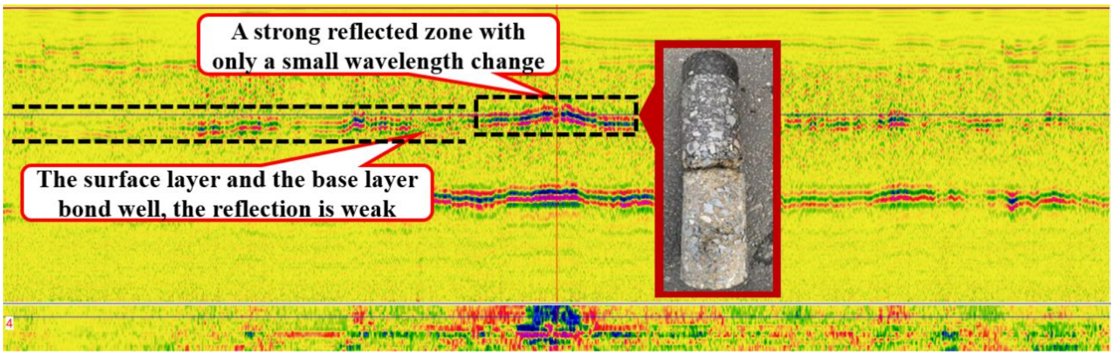

Figure 6. Radar Images Characteristics of Debonding Between Layers and Corresponding Core

(3) Voids

The area with voids is usually larger than that with interlayer bonding defect. The internally filled air or water medium covers a certain three-dimensional space, and the waveform of the distress area shows regular strong reflection, which has greater influence in the vertical range. Therefore, the phase axis is easy to dislocate.

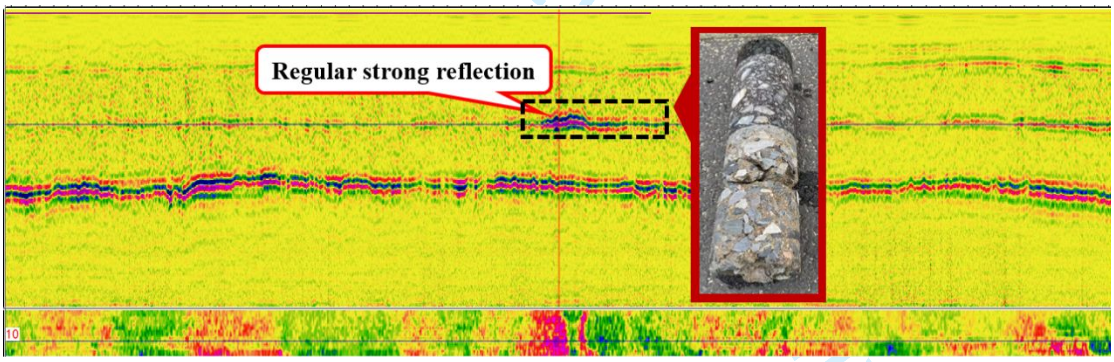

Figure 7. Radar Images Characteristics of Voids and Corresponding Core

(4) Cracks

The main form of cracks is transverse and longitudinal cracks. Due to the existence of different media such as water or air in the cracks, the reflected waveforms show obvious waveform changes in the radar spectrum. The phase axis is discontinuous, with part of continuous vertical hyperbolic shape, forming a local strong reflection.

324 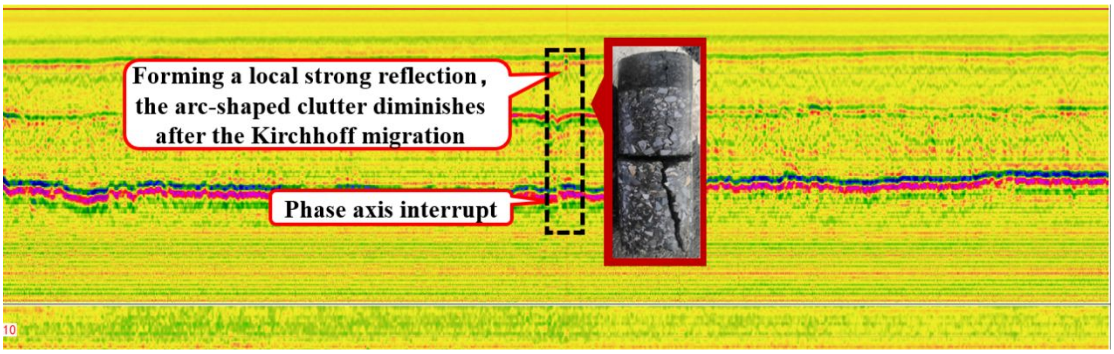

325 Figure 8. Radar Images Characteristics of Cracks and Corresponding Core

326

327 **4. 3D digital modeling method for internal road surface distress**

328 The three-dimensional digital imaging method is essentially an interpolation operation
329 on the radar signal dataset, which fits high-resolution and high-precision features of
330 defects based on the dataset, and requires adding one or more offset support points for
331 each signal feature point. To ensure the accuracy of signal details and solve the
332 problem of reconstructing sparse dataset defect features, this article combines the
333 inverse distance weighting interpolation method, ray-casting algorithm, and trilinear
334 interpolation method based on the principle of radar signal dataset construction to
335 achieve fast interpolation and improve the resolution of three-dimensional defect
336 models.

337 ***4.1 Principles of radar signal dataset construction***

338 Constructing a 3D point scattering signal data set based on the original radar data is
339 the basis for establishing a 3D digital model. The direction of transmitting antenna,
340 that is, the cross-sectional direction, is defined as x direction according to the interval
341 of receiving antenna iR; the radar advancing directing, i.e., the long-sectional

direction, is defined as the y direction according to the sampling interval. The sampling interval is 1.72cm, which means that antenna transmits a signal downward every 1.72cm. The number of channels is continuously accumulated by sampling interval, and the starting number of channels is defined as the three-dimensional coordinate origin, which in turn forms the XOY plane with 14 test channels and the continuous sampling intervals, as shown in Figure 9.

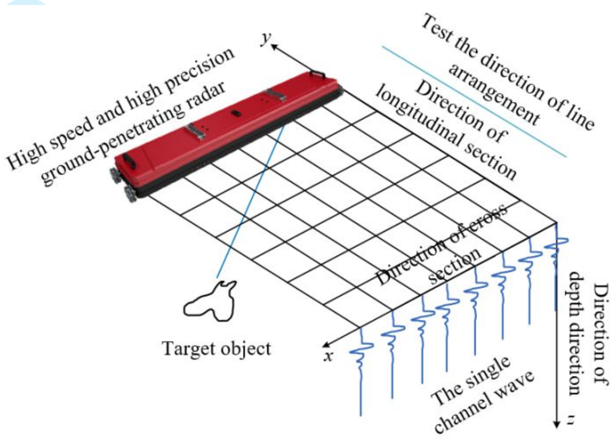

Figure 9. Coordinate System of Measured Data Acquisition

The electromagnetic echo signal received by each test channel of the array radar is an electric field intensity waveform profile consisting of row vectors. After pre-processing the echo signals corresponding to the characteristic lesions in the order described in Section 2.1, a two-dimensional matrix [number of channels, electric field intensity] consisting of all the processed channels was obtained. The 3D array radar can obtain 14 A-scan single-channel waveforms at the same spatial mileage position and 14 B-scan sections in the direction of longitudinal section at the same time. The A-scan direction (the depth direction) is defined as the Z-direction. The effective test depth of 900MHz array radar is about 100cm and the sampling points of the single-channel waveform are 256 points, so this paper divided the Z-direction by

100cm/256≈0.4cm equal interval. The electric field intensity, corresponding to the feature points, was transposed into a one-dimensional single-column matrix. The XOY plane was combined with the feature points and electric field intensity data to build a three-dimensional matrix consisting of three-dimensional coordinates and electric field intensity. This three-dimensional matrix is the point scattering signal data set composed of electric field signals for the characteristic distress.

4.2 Spatial interpolation of signal dataset

The dataset is only a data array composed of C-scans, which is finally presented as a 3D data body in the form of a combination of 14 B-scans. It is difficult to form a complete entity imaging due to the sparse data density. Therefore, in order to present the internal pavement distress more comprehensively, fully retain the distress features while enhancing the correlation between the measured data and effectively use the measured data, it is necessary to choose a suitable spatial interpolation method to spatially interpolate and densify the signal dataset.The spatial interpolation method based on GIS technology is currently the most common method for the rational use of geological data and the study of geological properties (Zuo, 2020). Spatial interpolation was performed based on the relationship between the attribute values of sample points and their spatial locations, and then the analysis from "point" to "surface" was realized. Therefore, based on the three-dimensional matrix, composed of data sections, and the radar characteristics including target scattering characteristics consistency, fusion processing phase consistency, a three-dimensional digital model of pavement distress was built from the spatial data distribution characteristics, gridded data morphology, spatial interpolation, etc.

The electric field strength data has a certain spatial correlation. The closer the spatial distance between two points, the more similar their property values are, and conversely, the further the distance, the less likely their property values are similar. Therefore, the inverse distance weighting (IDW) method was used for spatial interpolation, which is suitable for spatially autocorrelated measurements with few selection conditions, low complexity, and fast processing speed. Samples of known points within the search radius were used to estimate the value of unknown points, and each location corresponds to a predicted value. The generated surface can pass through all sample points, and a grid set of pavement internal distress data was obtained, which is uniformly distributed and dense enough to reflect local differences. The principle is as follows:

$$Z_0 = \frac{\sum_{i=1}^{n} \frac{z_i}{d_i^k}}{\sum_{i=1}^{n} \frac{1}{d_i^k}} \tag{6}$$

where Z_0 is the estimated value of the point 0 to be interpolated; Z_i is the property value of known point i; d_i is the distance between the known point i and point 0; k is a determined power, generally taken as 1 or 2, and the larger the value, the greater the weight of the closer points; n is the number of known points used for the calculation.

4.3 Fast 3D interpolation and reconstruction algorithm for distress

Ray-casting algorithm is a widely used surface 3D reconstruction algorithm in the field of scientific visualization , which has achieved great success in fields such as medical imaging, seismic detection, and ocean detection due to its high drawing accuracy (Duan et al., 2023). The algorithm starts from a certain data point and emits a ray along the exit direction. The ray traverses the interior of the dataset for equidistant resampling, and assigns optical properties (such as color value and opacity) to all sampled points using interpolation algorithms. The color values of the sampled points on the ray are then synthesized in order from front to back or from back to front, until the accumulated color value exceeds the set threshold, from which the color value of the corresponding pixel point of the ray is obtained. Finally, the algorithm traverses all points in the dataset to complete the 3D reconstruction of the distress. The above process is mainly divided into processes such as data value classification according to threshold, color value and opacity assignment, resampling, interpolation calculation, and image synthesis, as shown in Figure 10.

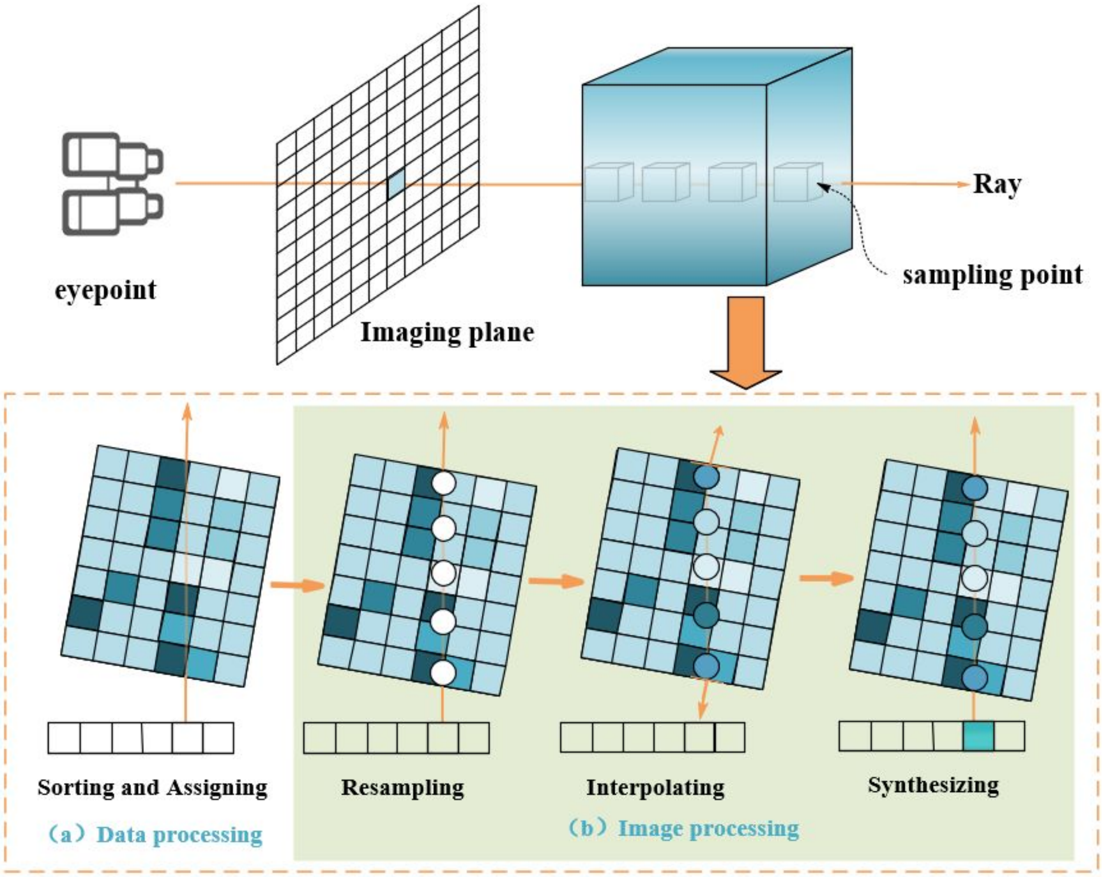

Figure 10. Principle of Ray Projection Algorithm

The ray-casting algorithm requires three threshold values to be calibrated for the interested and observed parts: the environment where the observed object is located, the transition layer, and the observed object itself. A high opacity value is assigned to the observed object to make it clearly visible and obtain the internal information structure of the data. To reduce the spatial resolution loss caused by the inverse distance weighting method and achieve prominent display of distress areas, this article divides the three thresholds based on waveform characteristics such as electromagnetic wave amplitude and phase, and images them to different color values (RGB) and opacity values (Alpha). The internal pavement distress three-dimensional digital model with high identification is obtained by assigning green to the pavement environment, yellow to the transition layer, and red to the distress. The amplitude discrete data range of the 3D array ground- penetrating radar used in this detection is $\pm 2^{15} N/C$, that is, $E_{max} = 32768$, $E_{min} = -32768$. Using the conclusion obtained in section 3.2 and taking Figure 10 as an example, the B-scan images in the YOZdirection where the distress is located is extracted, and the positions of five regions in the images with strong waveform changes, such as regions ①②③④⑤ in Figure 11, are calibrated. The maximum value of the radar signal$|E_{i\,max}|$ at that position is used as the threshold value for segmentation, where the maximum values of each region are$|E_{1max} = 28550|$, $|E_{2max}| = 17032|$, $|E_{3max}| = 15643|$, $|E_{4max}| = 13581|$ and $|E_{5max}| = 12756$ respectively. In addition, I, II, III, and IV in Figure 12 represent the positions of the interface between the upper and middle layers, the interface between the surface layer and the base layer, the upper and lower base layers, and the interface between the base layer and the subgrade respectively, and their corresponding electromagnetic signals. The imaging plane formed by the segmentation based on the above thresholds in the XOY direction is shown in Figure 12.

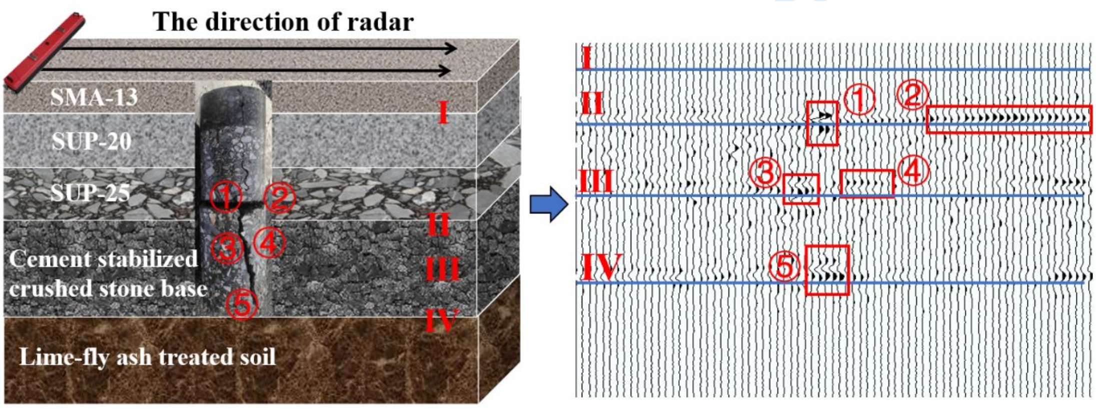

Figure 11. Threshold Calibration of Actual Detected Data

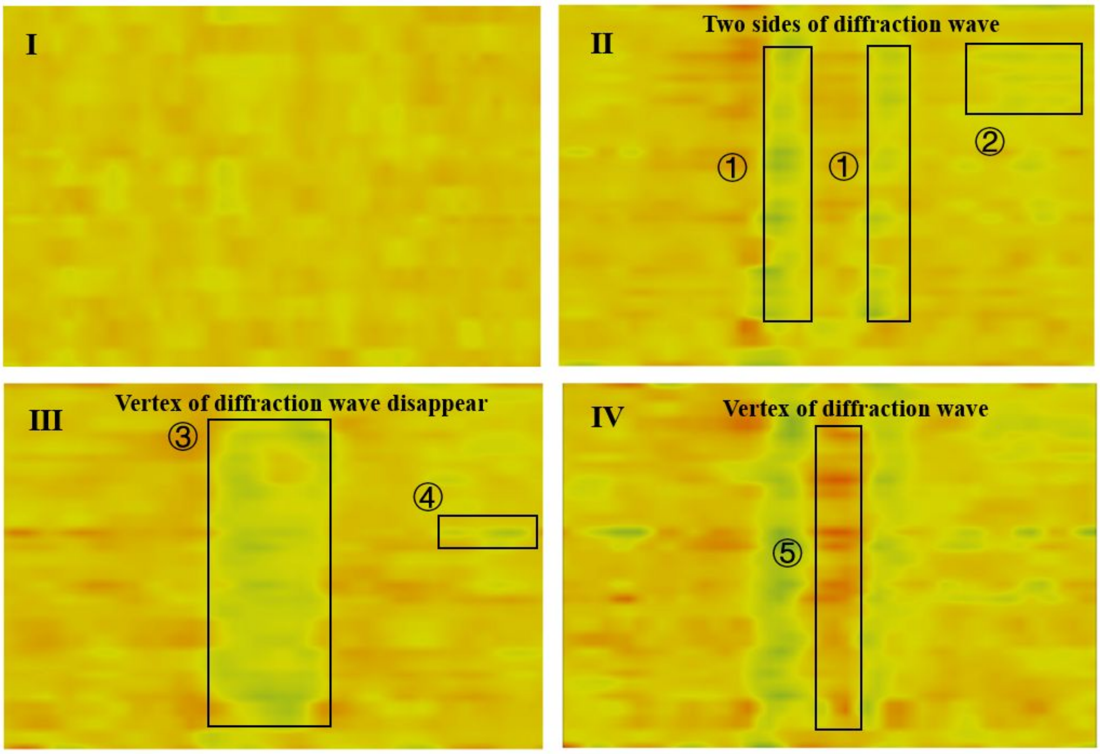

Figure 12. Imaging Planes with Different Thresholds

The imaging plane obtained by dividing the threshold as described above is resampled. Data interpolation during the resampling process is crucial to improving the imaging quality of the algorithm. Trilinear interpolation is used in this paper. Trilinear interpolation was performed on a tensor product grid of 3D discrete sampled data. Assuming that the color values vary linearly along the three coordinate axis directions, appropriate calculation regarding the values of (x, y, z) was carried out linearly on the local rectangular prism, through the data points on the grid. Since the antennas were not uniformly laid out, the 3D data grid set is also not distributed uniformly. The rays projected into the 3D parameter space were sampled equidistantly, and the color values of the new sampling points are obtained by trilinear interpolation of the color values and opacity of the eight original data points nearest to the new sampling points, as shown in Figure 13. In addition, the interpolation results were not related to the order of interpolation calculation. By this method, the correlation between radar data at each sampling point location can be effectively reflected, thus displaying spatial pattern of distress data effectively. The final constructed 3D digital model of the distress is shown in Figure 14 below. Its principle is as follows:

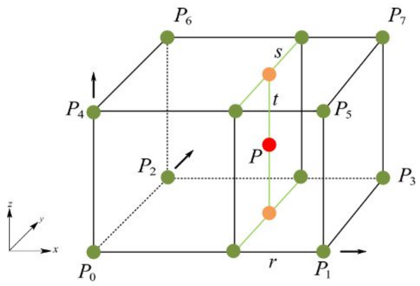

Figure 13. Trilinear Interpolation Principles

$$d_p = \frac{rst}{xyz} d_{p_0} + \frac{st}{yz}\left(1-\frac{r}{x}\right) d_{p_1} + \frac{rt}{xz}\left(1-\frac{s}{y}\right) d_{p_2} + \frac{t}{z}\left(1-\frac{r}{x}\right)\left(1-\frac{s}{y}\right) d_{p_3} + \frac{rs}{xy}\left(1-\frac{t}{z}\right) d_{p_4} + \frac{s}{y}\left(1-\frac{r}{x}\right)\left(1-\frac{t}{z}\right) d_{p_5} + \frac{r}{x}\left(1-\frac{s}{y}\right)\left(1-\frac{t}{z}\right) d_{p_6} + \left(1-\frac{r}{x}\right)\left(1-\frac{s}{y}\right)\left(1-\frac{t}{z}\right) d_{p_7} \quad (7)$$

where d_p is the color value of p point; the distance between p_0 and p_1 is represented as x; the distance between p_0 and p_2 is y; the distance between p_0 and p_4 is denoted as z; then the weight of p_0 is r/x; the weight of p_1 is (1 - r/x). Similarly, the weights of other vertices can be obtained.

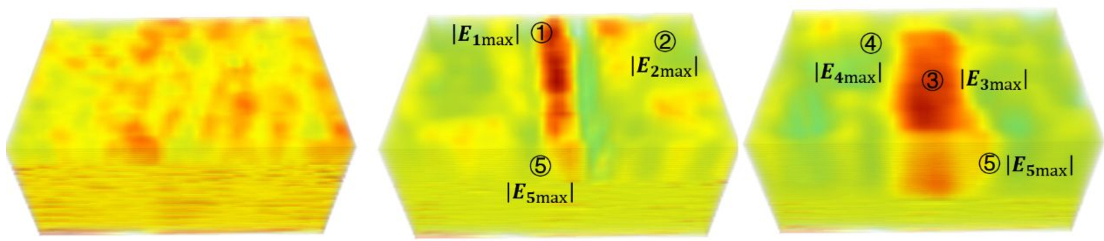

(a)Thresholds are not classified (b) $|E_{1max}|$、$|E_{2max}|$ and $|E_{5max}|$ (c) $|E_{3max}|$、$|E_{4max}|$ and $|E_{5max}|$

Figure 14. Different Threshold Values Correspond to 3D Digital Models of Distress

Based on the results shown in Figure 14 and extensive engineering practices, it is known that directly modeling of the radar signal data set as shown in (a) does not clearly highlight the internal features of pavement defects. If the middle position of the defect is used as shown in (c), with $|E_{imax}|$ between areas ③④⑤ of the upper and lower layers as the threshold, the characteristics of the defect itself are distorted due to the influence of the energy of the upper and lower diffraction waves. If the top position where the defect occurs is used as shown in Figure (b), with $|E_{imax}|$ in areas ①②⑤ as the threshold, the top and bottom diffraction wave characteristics of the defect can be well highlighted, resulting in a clear visualization of the internal pavement defects. Therefore, using $|E_{i\,max}|$ in the areas where the waveform changes sharply between the surface layer and the base layer and between the base layer and the subgrade as the thresholds, and combining the ray projection method with data interpolation, a clear and intuitive three-dimensional digital model of pavement defects can be constructed.

Two commonly used interpolation methods are nearest neighbor interpolation and trilinear interpolation. Therefore, the imaging effects of the two interpolation methods were compared as shown in Figure 15. Nearest neighbor interpolation has a small calculation amount, but the interpolated image has discontinuous gray levels and obvious sawtooth phenomena. Trilinear interpolation takes into account the distances between the interpolation point and each vertex of the voxel during the calculation process. Although it is slower, its accuracy is higher than that of nearest neighbor interpolation, which proves the effectiveness of using this method.

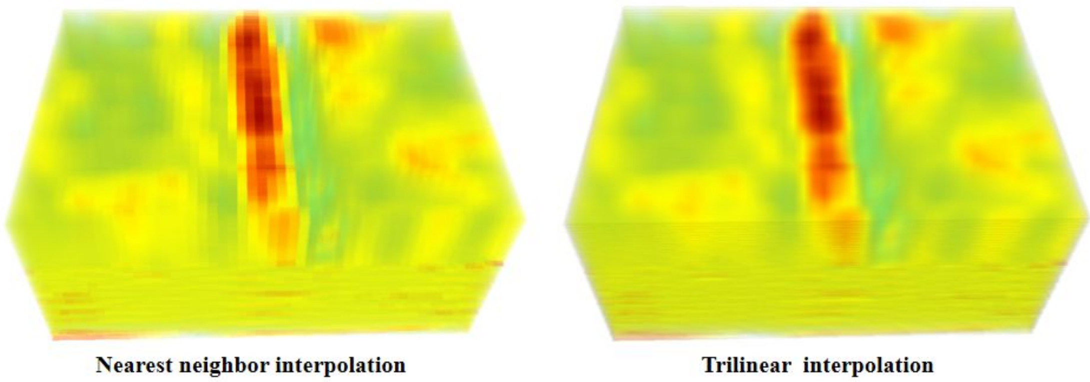

Figure 15. Imaging effect of different interpolation methods

5. Case study

In this paper, according to the radar images measured on a highway in Jiangsu Province, the number of roads corresponding to the characteristic distress was located and intercepted, and four typical distress were selected: cracks, loosening, voids, and debonding between layers. Through the above data processing and modeling methods, 3D digital models of pavement internal distress can be established, as shown in Figure 16-19.

Combined with the coring results, it can be seen that the 3D model can accurately image the reflection of the electromagnetic signal arriving at the lesion and completely present the global characteristics of the internal lesion. It fully compensates for the limitations of coring and helps to finely identify various distress types and their extent, thus providing a more accurate evaluation of the internal distress condition of the pavement. The 3D models show that the electromagnetic signal is strongest at the top and bottom of both the voids and loosening, and at the top of the cracks, while the energy of the signal is relatively weak at the position of the boundary diffraction waves. Taking Figure. 15-A (2) and C (2) as examples, it can be extrapolated from the 3D digital model of cracks that secondary microcrack cracks occur during the development of the main crack. The results are consistent with coring verification results, thus validating the effectiveness of the model.

It should also be noted that the model was constructed based on radar reflected wave signal data, which can initially determine the depth and size of the distress. The reliability of detection and identification was verified by field core extraction. The 3D digital model still needs to be based on the complete distress signals to reflect the real global characteristics of the pavement internal distresses. Therefore, this method is more effective for the data signal of 3D ground-penetrating radar. If 2D radar signals containing distress information are spliced together, a complete distress digital model can also be formed.

However, there is a discrepancy between the virtual distress size from the model and the actual physical size of the distress. Currently, it is a common technical challenge for researchers to model the quantitative characterization relationship between the numerical identification and the real state, and the characterization relationship will also facilitate the quantification of the material's performance changes, as the Walubita authors will quantify the fatigue characterization of HMAC mixes (Walubita et al., n.d.) and develop the corresponding standard guidelines in the future(Sanchez-Cotte et al., 2020).

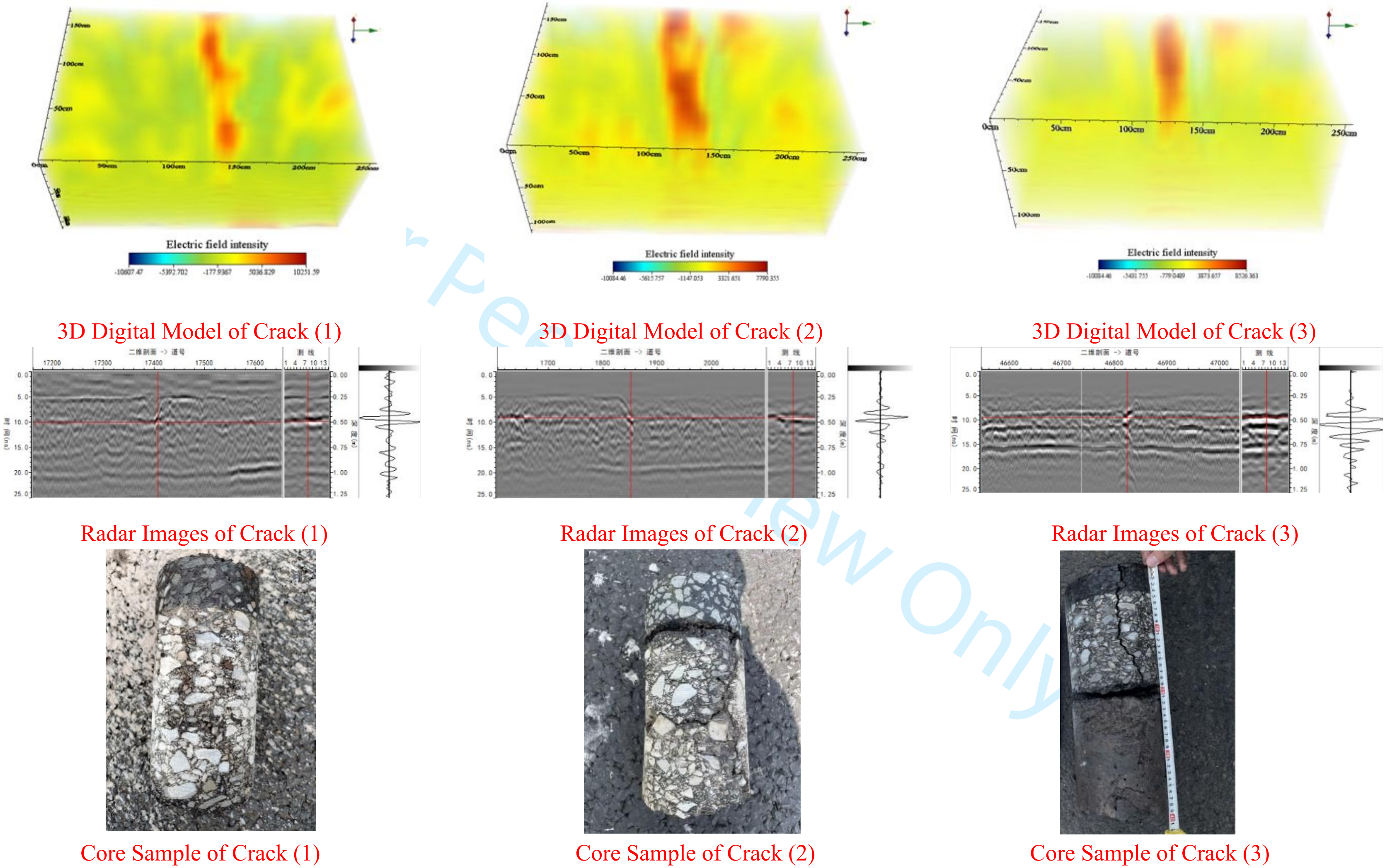

Figure 16. 3D Digital Models of Measured Cracks, Corresponding Radar Profiles, and Core Samples

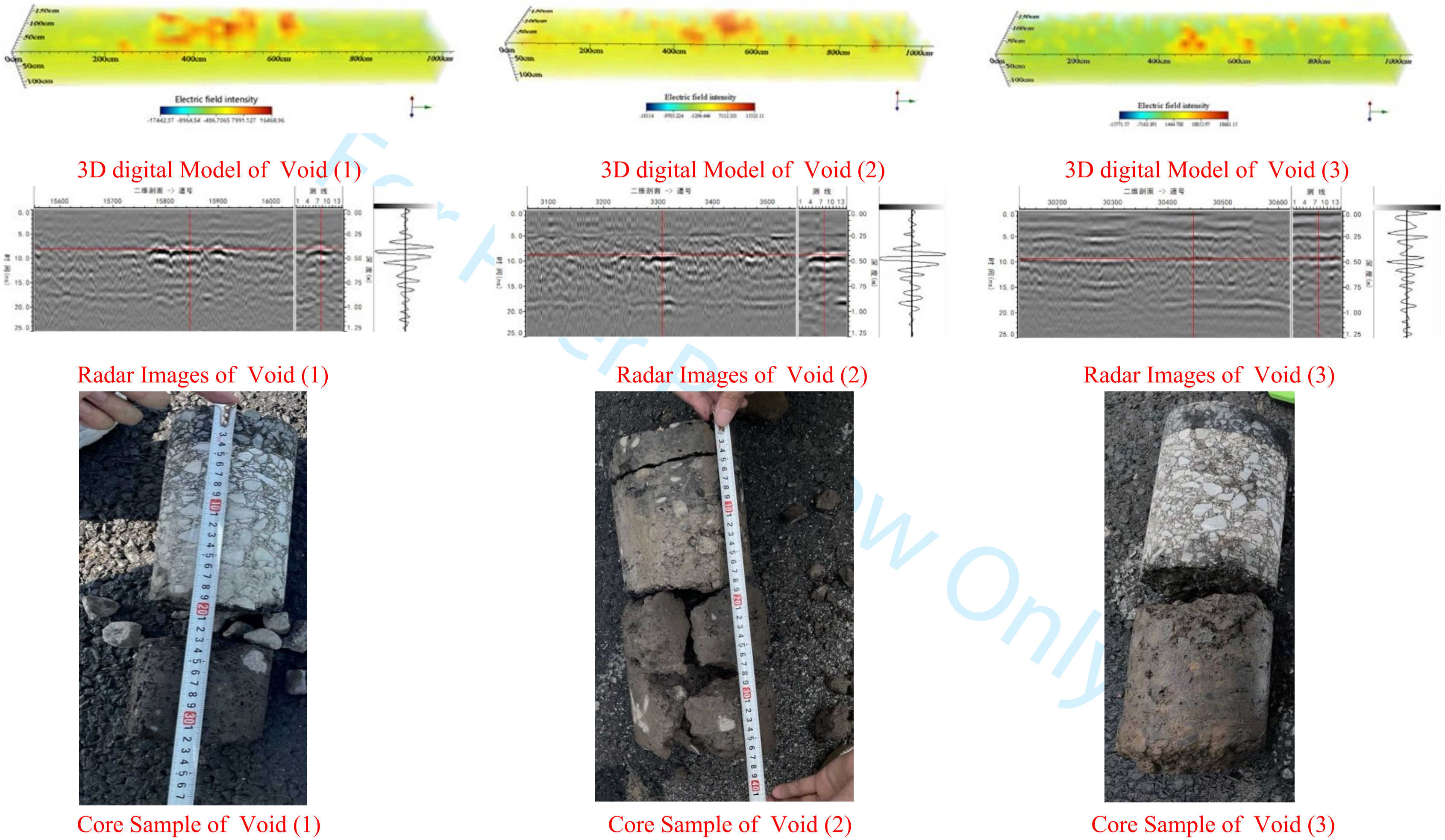

Figure 17. 3D Digital Models of Measured Voids, Corresponding Radar Profiles, and Core Samples

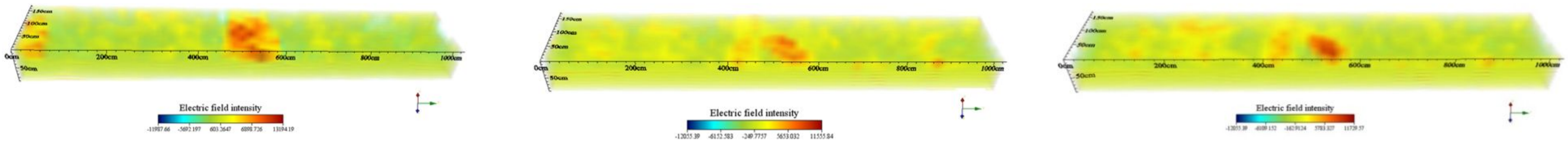

3D digital Model of Loosening (1) 3D digital Model of Loosening (2) 3D digital Model of Loosening (3)

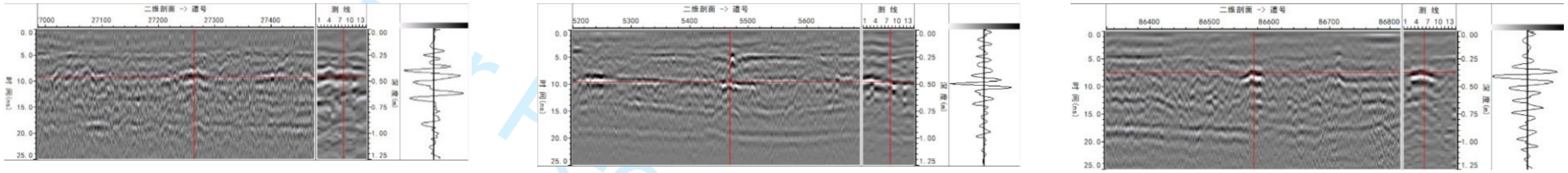

Radar Images of Loosening (1) Radar Images of Loosening (2) Radar Images of Loosening (3)

Core Sample of Loosening (1) Core Sample of Loosening (2) Core Sample of Loosening (3)

Figure 18. 3D Digital Models of Measured Loosening, Corresponding Radar Profiles, and Core Samples

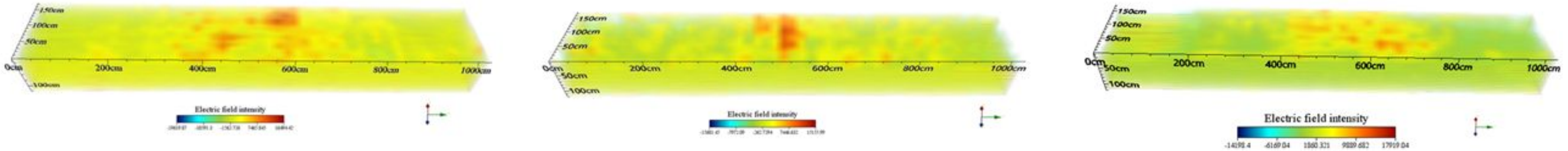

3D digital Model of Debonding (1) 3D digital Model of Debonding (2) 3D digital Model of Debonding (3)

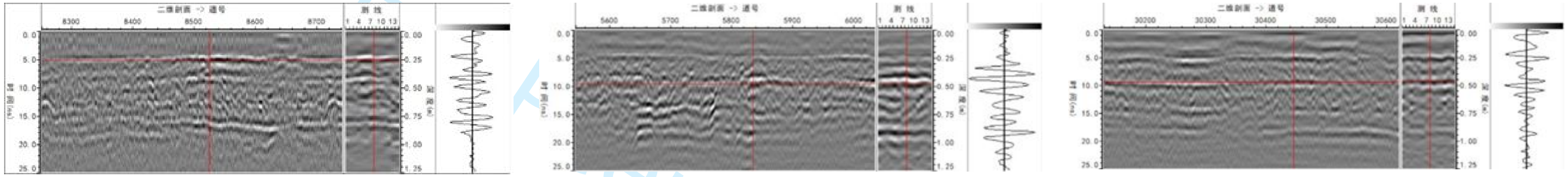

Radar Images of Debonding (1) Radar Images of Debonding (2) Radar Images of Debonding (3)

Core Sample of Debonding (1) Core Sample of Debonding (2) Core Sample of Debonding (3)

Figure 19. 3D Digital Models of Measured Debonding, Corresponding Radar Profiles, and Core Samples

6. Conclusions

The 3D array ground-penetrating radar signal measured over 1000km highway is the research basis of this paper. In this paper, the present mature radar signal preprocessing algorithm is combined with the ray projection algorithm and the trilinear interpolation algorithm in the field of three-dimensional imaging, to obtain clear radar images of typical distress, and to build a three-dimensional digital model of the internal distress of the pavement. The main findings are summarized below:

(1) Finite impulse response bandpass filtering and Kirschhoff migration method were used to pre-process the raw multi-channel electromagnetic signal data to enhance the signal characteristics of internal pavement distress. The radar images of crack distress show a continuous vertical multi-arc curve because cracks develop in the direction of pavement depth. In the same depth range of the pavement, the damage area of other distresses, such as poor interlayer debonding, loosening and void, is large. Therefore, the in-phase axis of the radar images of these distresses have some obvious characteristics, and the poor interlayer bonding radar images shows that the in-phase axis is a continuous and horizontal wave. Loosening fragmentation radar images is characterized by in-phase axon-floc disorder and reflection clutter. The cavitation is manifested as the dislocation of the in-phase axis.

(2) To establish a three-dimensional digital model that can visually present the physical characteristics of the distress, the inverse distance weighting method was

577 used to spatially interpolate the electromagnetic echo signal data set, and the radar
578 signal was divided by threshold using the ray projection method. The colour value and
579 opacity of all data points were calculated using the trilinear interpolation method. The
580 models show that the electromagnetic signal is strongest at the top and bottom of both
581 the voids and loosening, and at the top of the cracks, while the energy of signal is
582 weak at the boundary diffraction waves. The coring results from an engineering
583 project show that the 3D digital models of pavement internal distress can not only
584 help to visually present the distress and accurately determine the type of distress, but
585 also specifically show the relevant secondary distress.

586 (3) The established 3D digital models of pavement internal distresses can obtain the
587 interactive images between the pavement entity and the digital world, to accurately
588 identify multiple distress types and their scope. These models can lay the foundation
589 for accurately evaluating the internal pavement structure and tracking the dynamic
590 development pattern of the distress. It can also provide support for the road
591 maintenance decision of the whole life cycle.

592 These characteristics of distress atlas will provide the basis for distress recognition
593 in the future. The three-dimensional digital model of distress can effectively solve the
594 problem that the distress images of pavement interior is difficult to interpret and not
595 intuitive. In addition, the effects of the most widely used trilinear interpolation and the
596 nearest proximity method on the imaging effect are compared, and it is proved that the
597 trilinear interpolation algorithm can get a clearer three-dimensional digital model of the
598 distress. The establishment of 3D distress model also confirms that the 3D imaging

method commonly used in digital twin-based technology can enhance the readability of radar signal, and effectively fill the research gap in the field of pavement internal distress recognition. It should be noted that converting electromagnetic information into optical information, that is, establishing an accurate quantitative transformation relationship between virtual distress size and real physical size, is a difficult problem in this field and will be an important research content in the future.

References：

Ameri, M., Kashani Novin, M., & Yousefi, B. (2014). Comparison of the field measurements of asphalt concrete densities obtained by ground-penetrating radar, pavement quality indicator and the borehole coring methods. *Road Materials and Pavement Design*, *15*(4), 759–773. https://doi.org/10.1080/14680629.2014.909874

Breysse, D. (Ed.). (2012). *Non-Destructive Assessment of Concrete Structures: Reliability and Limits of Single and Combined Techniques: State-of-the-Art Report of the RILEM Technical Committee 207-INR*. Springer Netherlands. https://doi.org/10.1007/978-94-007-2736-6

Cruz, H., Raheem, A. A., & Nazarian, S. (2022). Digital Twin Technology Applications for Transportation Infrastructure—A Survey-Based Study. *Computing in Civil Engineering 2021*, 350–357. https://doi.org/10.1061/9780784483893.044

Dong, S., Hao, P., & Tighe, S. L. (2019). A diagnostic method for evaluating the condition index of cement-stabilised base using T-S fuzzy neural network. *International Journal of Pavement Engineering*, *20*(10), 1140–1153.

https://doi.org/10.1080/10298436.2017.1394097

Duan, X., Sun, Y., & Wang, J. (2023). ECA-UNet for coronary artery segmentation and three-dimensional reconstruction. *Signal, Image and Video Processing*, *17*(3), 783–789. https://doi.org/10.1007/s11760-022-02288-y

Forte, E., Mocnik, A., Basso, P., Casagrande, G., Martinucci, D., Pillon, S., Possamai, M., & Zambrini, R. (2021). Optimised Extraction of Archaeological Features from Full 3-D GPR Data. *Applied Sciences*, *11*(18), 8517. https://doi.org/10.3390/app11188517

Guo, S., Xu, Z., Li, X., & Zhu, P. (2022). Detection and Characterization of Cracks in Highway Pavement with the Amplitude Variation of GPR Diffracted Waves: Insights from Forward Modeling and Field Data. *Remote Sensing*, *14*(4), 976. https://doi.org/10.3390/rs14040976

Holopainen, M., Saunila, M., Rantala, T., & Ukko, J. (2022). Digital twins' implications for innovation. *Technology Analysis & Strategic Management*, 1–13. https://doi.org/10.1080/09537325.2022.2115881

Hou, Y., Li, Q., Zhang, C., Lu, G., Ye, Z., Chen, Y., Wang, L., & Cao, D. (2021). The State-of-the-Art Review on Applications of Intrusive Sensing, Image Processing Techniques, and Machine Learning Methods in Pavement Monitoring and Analysis. *Engineering*, *7*(6), 845–856. https://doi.org/10.1016/j.eng.2020.07.030

Hugenschmidt, J., & Herlyn, A. (2014). Damages in pavements caused by previous excavation work? *Proceedings of the 15th International Conference on Ground Penetrating Radar*, 852–856. https://doi.org/10.1109/ICGPR.2014.6970548

Kassem, E., Walubita, L., Scullion, T., Masad, E., & Wimsatt, A. (2008). Evaluation of Full-

Depth Asphalt Pavement Construction Using X-Ray Computed Tomography and Ground Penetrating Radar. *Journal of Performance of Constructed Facilities*, *22*(6), 408–416. https://doi.org/10.1061/(ASCE)0887-3828(2008)22:6(408)

Lee, S., Park, J.-J., & Cho, B. H. (2022). Management of cavities under flexible pavement road network in metropolitan area: Detection, evaluation, and rehabilitation. *Developments in the Built Environment*, *12*, 100091. https://doi.org/10.1016/j.dibe.2022.100091

Li, J., Walubita, L. F., Simate, G. S., Alvarez, A. E., & Liu, W. (2015). Use of ground-penetrating radar for construction monitoring and evaluation of perpetual pavements. *Natural Hazards*, *75*(1), 141–161. https://doi.org/10.1007/s11069-014-1314-1

Li, J., Yin, G., Wang, X., & Yan, W. (2022). Automated decision making in highway pavement preventive maintenance based on deep learning. *Automation in Construction*, *135*, 104111. https://doi.org/10.1016/j.autcon.2021.104111

Liu, Z., Gu, X., Yang, H., Wang, L., Chen, Y., & Wang, D. (2022). Novel YOLOv3 Model With Structure and Hyperparameter Optimization for Detection of Pavement Concealed Cracks in GPR Images. *IEEE Transactions on Intelligent Transportation Systems*, *23*(11), 22258–22268. https://doi.org/10.1109/TITS.2022.3174626

Menon, D., Anand, B., & Chowdhary, C. L. (2023). Digital Twin: Exploring the Intersection of Virtual and Physical Worlds. *IEEE Access*, *11*, 75152–75172. https://doi.org/10.1109/ACCESS.2023.3294985

Morsy, S., & Shaker, A. (2022). Evaluation of LiDAR-Derived Features Relevance and Training Data Minimization for 3D Point Cloud Classification. *Remote Sensing*, *14*(23), 5934. https://doi.org/10.3390/rs14235934

Pereira, M., Burns, D., Orfeo, D., Zhang, Y., Jiao, L., Huston, D., & Xia, T. (2020). 3-D Multistatic Ground Penetrating Radar Imaging for Augmented Reality Visualization. *IEEE Transactions on Geoscience and Remote Sensing*, *58*(8), 5666–5675. https://doi.org/10.1109/TGRS.2020.2968208

Rasol, M., Pais, J. C., Pérez-Gracia, V., Solla, M., Fernandes, F. M., Fontul, S., Ayala-Cabrera, D., Schmidt, F., & Assadollahi, H. (2022). GPR monitoring for road transport infrastructure: A systematic review and machine learning insights. *Construction and Building Materials*, *324*, 126686. https://doi.org/10.1016/j.conbuildmat.2022.126686

Sanchez-Cotte, E. H., Fuentes, L., Martinez-Arguelles, G., Rondón Quintana, H. A., Walubita, L. F., & Cantero-Durango, J. M. (2020). Influence of recycled concrete aggregates from different sources in hot mix asphalt design. *Construction and Building Materials*, *259*, 120427. https://doi.org/10.1016/j.conbuildmat.2020.120427

Saponaro, P., Sherbondy, K., & Kambhamettu, C. (2014). Concealed Target Detection with Fusion of Visible and Infrared. In G. Bebis, R. Boyle, B. Parvin, D. Koracin, R. McMahan, J. Jerald, H. Zhang, S. M. Drucker, C. Kambhamettu, M. El Choubassi, Z. Deng, & M. Carlson (Eds.), *Advances in Visual Computing* (Vol. 8888, pp. 568–577). Springer International Publishing. https://doi.org/10.1007/978-3-319-14364-4_55

Sivagnanasuntharam, S., Sounthararajah, A., Ghorbani, J., Bodin, D., & Kodikara, J. (2023). A state-of-the-art review of compaction control test methods and intelligent compaction technology for asphalt pavements. *Road Materials and Pavement Design*, *24*(1), 1–30. https://doi.org/10.1080/14680629.2021.2015423

Soldovieri, F., Hugenschmidt, J., Persico, R., & Leone, G. (2007). A linear inverse scattering algorithm for realistic GPR applications. *Near Surface Geophysics*, *5*(1), 29–41. https://doi.org/10.3997/1873-0604.2006016

Syeda, R. Z., Savelyev, T. G., van Beurden, M. C., & Smolders, A. B. (2021). Sparse MIMO Array for Improved 3D mm- Wave Imaging Radar. *2020 17th European Radar Conference (EuRAD)*, 342–345. https://doi.org/10.1109/EuRAD48048.2021.00094

Tello-Cifuentes, L., Marulanda, J., & Thomson, P. (2023). Detection and classification of pavement damages using wavelet scattering transform, fractal dimension by box-counting method and machine learning algorithms. *Road Materials and Pavement Design*, 1–19. https://doi.org/10.1080/14680629.2023.2219338

Thelen, A., Zhang, X., Fink, O., Lu, Y., Ghosh, S., Youn, B. D., Todd, M. D., Mahadevan, S., Hu, C., & Hu, Z. (2022). A comprehensive review of digital twin — part 1: Modeling and twinning enabling technologies. *Structural and Multidisciplinary Optimization*, *65*(12), 354. https://doi.org/10.1007/s00158-022-03425-4

Walubita, L. F., Martin, A. E., Jung, S. H., Glover, C. J., Park, E. S., & Chowdhury, A. (n.d.). *Comparison of Fatigue Analysis Approaches for Two Hot Mix Asphalt Concrete (HMAC) Mixtures*.

Walubita, L. F., Scullion, T., Leidy, J., & Liu, W. (2009). Non-Destructive Testing Technologies: Application of the Ground Penetrating Radar (GPR) to Perpetual Pavements. *Road Materials and Pavement Design*, *10*(2), 259–286. https://doi.org/10.1080/14680629.2009.9690195

Wang, S., & Al-Qadi, I. L. (2022). Impact and Removal of Ground-Penetrating Radar Vibration on Continuous Asphalt Concrete Pavement Density Prediction. *IEEE*

709 *Transactions on Geoscience and Remote Sensing*, *60*, 1–14.
710 https://doi.org/10.1109/TGRS.2021.3106041
711 Yan, K. (2022). Research on Highway Data Reconstruction Method of Three-
712 Dimensional Ground-Penetrating Radar. Lanzhou Jiaotong University.
713 DOI:10.27205/d.cnki.gltec.2022.000753.
714 Zhu, J., Zhao, D., & Luo, X. (2023). Evaluating the optimised YOLO-based defect detection
715 method for subsurface diagnosis with ground penetrating radar. *Road Materials and*
716 *Pavement Design*, 1–18. https://doi.org/10.1080/14680629.2023.2199880
717 Zhu, W., Huang, Q., Liu, L., & Ma, B. (2020). Three-Dimensional Reverse Time Migration
718 of Ground-Penetrating Radar Signals. *Pure and Applied Geophysics*, *177*(2), 853–865.
719 https://doi.org/10.1007/s00024-019-02341-x
720 Zuo, H. (2020). The construction of stratigraphic structure model in mining area under
721 virtual reality–geographic information system. *Arabian Journal of Geosciences*, *13*(17), 853.
722 https://doi.org/10.1007/s12517-020-05844-3
723